Convection-Induced Compositional Patterning at Grain Boundaries in Irradiated Alloys

G. F. Bouobda Moladje,[1] R. S. Averback,[1] P. Bellon,[1] and L. Thuinet[2]
[1]*Department of Materials Science and Engineering, University of Illinois at Urbana-Champaign, Urbana-Champaign, Illinois 61801, USA*
[2]*Université de Lille, CNRS, INRAE, Centrale Lille, UMR 8207–UMET–Unité Matériaux et Transformations, F-59000 Lille, France*

(Received 14 December 2022; accepted 13 July 2023; published 1 August 2023)

We consider the stability of precipitates formed at grain boundaries (GBs) by radiation-induced segregation in dilute alloys subjected to irradiation. The effects of grain size and misorientation of symmetric-tilt GBs are quantified using phase field modeling. A novel regime is identified where, at long times, GBs are decorated by precipitate patterns that resist coarsening. Maps of the chemical Péclet number indicate that arrested coarsening takes place when solute advection dominates over thermal diffusion right up to the precipitate-matrix interface, preventing interfacial local equilibrium and overriding capillary effects. This contrasts with liquid-solid mixtures where convection always accelerates coarsening.

DOI: 10.1103/PhysRevLett.131.056201

Materials systems subjected to external forcing are often observed to self-organize into patterns [1–4]. Instabilities arise in these systems that can trigger the formation of transient structures, which then evolve into metastable or even stable steady-state patterns. Such patterns have been reported in solids and alloys subjected to irradiation [5,6] and to severe plastic deformation [7–9], resulting in microstructures with emergent pattern length scales and symmetry. Notable examples of *defect* patterns are void, bubble, and walls of dislocations, which derive from anisotropic diffusion of point defects and defect clusters in irradiated crystals [10,11], and nanoscale *compositional* patterns in alloys, which are due to the nonlocal character of forced chemical mixing during irradiation or plastic deformation [12]. Convection can also trigger patterning, but this mechanism is traditionally studied in fluids, where hydrodynamic instabilities are often present [4]. In particular, random and turbulent [13–16] or chiral [17] shear flows in binary fluid mixtures promote domain stretching and breakup, resulting in arrested coarsening and steady-state patterning for large enough ratios of chemical convection to chemical diffusion, i.e., at high enough chemical Péclet number. For a system with uniform convection, $\mathrm{Pe} = (v d_{\mathrm{adv}})/D_B$ where v is the solute drag velocity, d_{adv} the advection distance and D_B the solute diffusion coefficient. In the case of solid particles in a fluid matrix, however, both experiments [18] and theory [19,20] indicate that convection only accelerates coarsening, even for a high Pe number. This latter observation can be rationalized by noting that solid particles in a fluid flow do not stretch or breakup, while convection promotes solute transport and particle coagulation. The role of chemical convection on the coarsening of solid particles in solid matrices has received much less attention, despite its relevance to various materials processes: the transport of ionic species in battery electrodes and electrolytes during charge and discharge cycles [21]; the chemical mixing forced by plastic deformation in crystalline alloys [7,22,23]; the transport of mass to surfaces in energetic displacement cascades [24–26]; and the flow of point defects to sinks under irradiation [4], the subject of this Letter. Using a simple model for point defect and chemical transport in an irradiated alloy, along with phase field simulations, we report on a novel compositional patterning phenomenon at grain boundaries (GBs) and show that it results from solute advection to GBs coupled with anisotropic solute diffusion at GBs. More specifically, we illustrate that arrested coarsening is a consequence of a high chemical Péclet number along the GBs, which overrides the effects of equilibrium capillary forces.

The generic microstructure investigated in this Letter consists of a flat grain boundary formed by two abutting grains in a dilute A-B alloy. Irradiation of this alloy produces isolated point defects homogeneously. These point defects, vacancies, and interstitials can then recombine or diffuse to the GB, which is treated as a perfect sink (see Sec. SI in Supplemental Material [27]). Continuous irradiation therefore establishes persistent point defect fluxes to the GB. For the alloy considered here, such point defect migration leads to solute advection to sinks through flux coupling, [28–30], i.e., point defects bind to solute atoms and "drag" them to sinks. This mechanism can also result in solute precipitation [28,31,32], although the conditions for precipitation, and its extent are difficult to anticipate *a priori*. Consider, for instance, the role of the GB separation distance, or equivalently the grain size, and that of the GB character. As the grain size increases the amount of solute available for segregation to the GB increases [33] but large grain sizes promote defect recombination far from the GB, thus limiting the actual amount of solute segregation. Furthermore, precipitation can be affected by the GB character since misfit dislocations act as nucleation sites for precipitation and GB structure and segregation affect solute diffusivity along the GB [34]. The central question of the present work is to determine the resulting precipitation microstructure and whether it can undergo self-organization under appropriate irradiation conditions. Phase field modeling is used for this purpose, since it can include the main physical processes relevant to irradiation and evolve systems of sufficient sizes over long timescales [35]. The state of the system is described by four phase field variables, X_V, X_I, X_A, and X_B, representing the molar fraction of vacancies, interstitials, solvent, and solute atoms, respectively. The kinetic evolution equations for these field variables are given by a kinetic phase-field model that includes radiation effects and flux coupling [36]:

$$\frac{\partial X_d}{\partial t} = \nabla.\sum_{\alpha}\sum_{\beta}\frac{l^d_{\alpha\beta}X_d}{k_B T}\left(\mathrm{sign}(d)\nabla\frac{\delta F}{\delta X_\beta} + \nabla\frac{\delta F}{\delta X_d}\right) + K_0 - K_R - K^d_s,$$

$$\frac{\partial X_\alpha}{\partial t} = \nabla.\sum_{d}\sum_{\beta}\frac{l^d_{\alpha\beta}X_d}{k_B T}\left(\nabla\frac{\delta F}{\delta X_\beta} + \mathrm{sign}(d)\nabla\frac{\delta F}{\delta X_d}\right) + \zeta_{\mathrm{noise}}, \tag{1}$$

where $\alpha, \beta = A$, B, and $d = V$, I with $\mathrm{sign}(V) = -1$ and $\mathrm{sign}(I) = 1$. K_0 represents the point defect production rate in displacements per atom (dpa) per second, T the temperature, K_R the mutual recombination rate between vacancies and interstitials, and K^d_s the point defect annihilation rate at GB sink is defined as $K^d_s = \lambda(\boldsymbol{x})[X_d(\boldsymbol{x}, t) - X^{\mathrm{eq}}_d]/\Delta t$ with $\lambda(\boldsymbol{x})$ taking values of 1 (respectively, 0) inside (respectively, outside) the sink capture area, X^{eq}_d the equilibrium defect concentration and Δt the integration time step. ζ_{noise} is a Gaussian random noise function simulating thermal fluctuations to suppress trapping in shallow metastable configurations. $(l^d_{\alpha\beta})$ represents the matrix of Onsager transport coefficients; it is symmetric, positive, and depends on the alloy temperature and composition. The total free energy of the system F includes local chemical interactions, and long-range elastic interactions. The chemical free energy is written as the sum of the free energy of the homogeneous alloy, using a regular solid solution model, and a gradient energy term accounting for heterogeneities in the concentration field of chemical species [36]. The elastic energy results from the interactions between point defects and sinks, and is calculated via microelasticity theory [37] by considering an elastically homogeneous medium. The strain energy due to the lattice misfit is neglected here for the sake of simplicity. Note that the second term on the rhs of the solute evolution equation Eq. (1) reduces to $l^d_{d\beta}\nabla X_d$ (see details in [27]). This second term in Eq. (1) is thus a drift, or convective, term that corresponds to an advection of solute atoms by the permanent fluxes of defects d. The atomic mixing forced by nuclear collisions induced by irradiation, i.e., ballistic mixing [38], is deliberately left out, so that pattern evolutions detailed below cannot be associated with such mixing. This is of note since previous modeling studies have indeed demonstrated that ballistic mixing can trigger compositional patterning in irradiated alloys [39–42]. For computational efficiency, the phase field equations for only B, V, I in Eq. (1) are solved, in 2D Cartesian coordinates (x_1, x_2), using a forward Euler method with an adaptive time step [36] (see Fig. S1 in Supplemental Material [27]).

Parameters for the model A-B immiscible alloy system investigated here mimic a dilute Al-Sb alloy, but mainly they were selected to promote strong flux coupling (see Supplemental Material [27], Sec. SI, Table S1, and Refs. [43–50]). Specifically, the large solute-vacancy binding energy $E^b_{\text{Sb-}V} = 0.3$ eV [51] results in a strong advection of the solute to the GB by vacancy fluxes at 300 K. The drag ratios of Onsager coefficients calculated by the transport coefficient code KINECLUE [52] are $l^V_{VB}/l^V_{BB} \approx 1$ and $l^V_{VB}/l^V_{VV} \approx 1$ (see Fig. S2 [27]). In contrast, interstitials do not promote Sb segregation since oversized solutes such as Sb in Al do not form mixed dumbbells; we thus set $l^I_{BB} = l^I_{AB} = 0$ in Eq. (1). The vacancy-driven solute-drag flux [the second term in the double summation in Eq. (1)] is opposed by a back diffusional flux (the first term in the double summation) once the solute depletion in the matrix drops below the equilibrium solubility limit, $X^{eq}_B = 1.75 \times 10^{-4}$ at $T = 300$ K. Note that the diffusion coefficient controlling this back flux is enhanced by the point defect supersaturation created by irradiation, and it is here referred to as D^{RED}_B. In addition to these fluxes, which are primarily perpendicular to the GB, solute is also mobile in the grain boundary.

Two different models for the GB were investigated. The first model corresponds to symmetric tilt grain boundaries (STGBs), modeled as an array of equally spaced edge dislocations. The misorientation θ of an STGB is related to the spacing between dislocation cores, h, as $h = b/2\sin(\theta/2)$, b being the magnitude of the Burgers vector. Misorientations from 2.4° ($h = 24b$) to 14.3° ($h = 4b$) were studied. Point defect concentrations

TABLE I. GB precipitate structures reached after an irradiation dose of 10 dpa, as a function of the grain size and the GB structure.

	Misorientation angle $\theta = b/h$				
d (nm)	2.38°	4.77°	9.55°	14.32°	Continuous sink
13.44 nm	◆	●	●	●	○
26.88 nm	◆	●	●	●	☆
40.32 nm	●	●	●	●	■
53.76 nm	●	●	●	∗	■
80.64 nm	●	●	●	■	■
94.08 nm	●	●	■	■	■
107.52 nm	●	■	■	■	■

■ solid flim; ∗ single precipitate; ●, ○ 2 precipitates; ☆ 3 precipitates; ◆ 4 precipitates.

within the GB capture region were held equal to bulk equilibrium values, $X_V^{\mathrm{eq}} = 1.5 \times 10^{-9}$ and $X_I^{\mathrm{eq}} \approx 0$, respectively. The capture zone was set to $4b$, corresponding to the dislocation core width [53]. The values of X_V^{eq} and X_I^{eq} are modified by the elastic strain field around the dislocation cores, see Fig. S3 [27], but this effect is relatively small. The solute diffusion coefficient along the GB, D_B^{GB}, is therefore approximately equal to $D_B^{b,\mathrm{eq}}$, the equilibrium bulk solute diffusion coefficient. The second type of GB used in the simulations mimics large angle GBs and relies on a continuum description, where the sink absorption region is a straight stripe of width $2b$.

Table I summarizes the microstructures reached at long times, here corresponding to an irradiation damage of 10 dpa, for various grain sizes. For the STGBs, solute concentration builds up around each dislocation core, leading eventually to solute-rich precipitates decorating each core. Two "trivial" structures can thus be expected at long times by comparing the precipitate diameter, d_p, to h: When $d_p < h$, e.g., $d = 13.44$ nm and $\theta = 2.38°$ in Table I, the precipitates do not overlap, resulting in a structure, hereafter referred to as type 1, where each dislocation core is decorated by one solute-rich precipitate; in contrast, when $d_p > h$, individual GB precipitates overlap and merge, eventually forming a continuous wetting precipitate layer along the GB, labeled as structure of type 2, e.g., $d \geq 80.64$ nm and $\theta = 14.32°$ in Table I (see also Fig. S4 [27]).

More interesting structures are observed for intermediate grain sizes and misorientations. These structures are composed of a finite number of precipitates, larger than 1 but smaller than the number of dislocation cores; see, for instance, $d \leq 80.64$ nm for $\theta = 9.55°$ in Table I. These GB structures, referred to as type 3 structures, developed differently for small and large misorientations. For small misorientations, type 3 structures began as type 1 structures that underwent partial coarsening with time, see Fig. 1, but coarsening became arrested at longer times. For larger misorientations, the type 3 structures were first continuous GB solute-rich films at low doses (<0.1 dpa), but precipitates subsequently formed by decomposition along the GB. The size of these precipitates, however, stabilized at long times, see Figs. 2 and 3. For continuous sinks, see last column in Table I, type 3 structures are again observed, following a mechanism very similar to that observed for large tilt boundary misorientations, i.e, spinodal-like decomposition along the GB and arrested coarsening. Decomposition occurs at larger doses (>1 dpa) for these boundaries, in comparison to STGBs, since it is not assisted by dislocation cores, see Fig. S5 [27]. Finite size effects and periodic boundary conditions were found to affect the exact linear density of precipitates found in type 3 structures, as expected (see Fig. S6) but not their main features nor their unexpected resistance to coarsening. We identify type 3 structures as GB compositional patterns since these structures are highly stable and the separation distance between precipitates presents an emergent length scale, distinct from the microscopic scales b and h, and the macroscopic scales set by the system sizes along x_1 and x_2.

The stability of selected type 3 structures was confirmed by increasing the irradiation dose to 30 dpa. For a structure

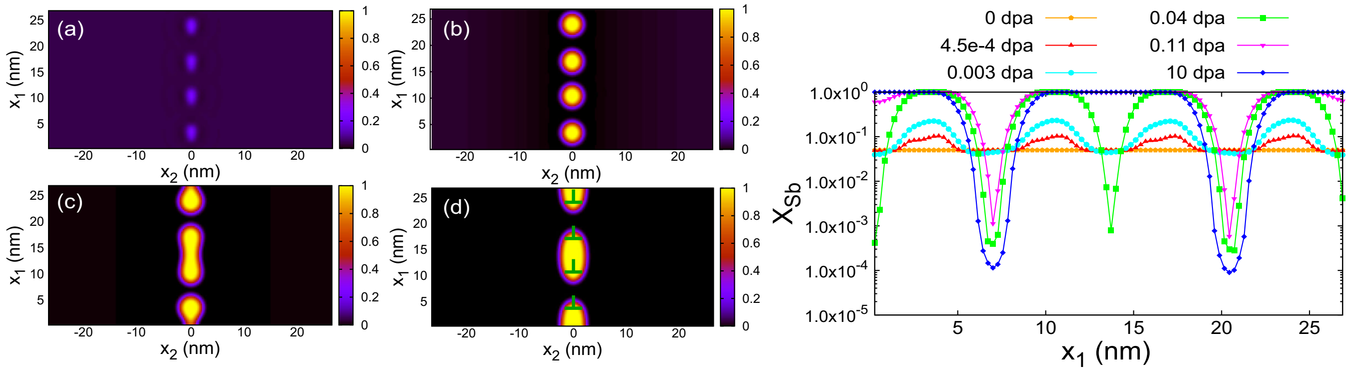

FIG. 1. Evolution of the Sb atomic fraction map for $\theta = 2.38°$ and $d = 53.76$ nm for (a) 0.003 dpa, (b) 0.04 dpa, (c) 0.11 dpa, (d) 10 dpa, and the corresponding profiles along the GB.

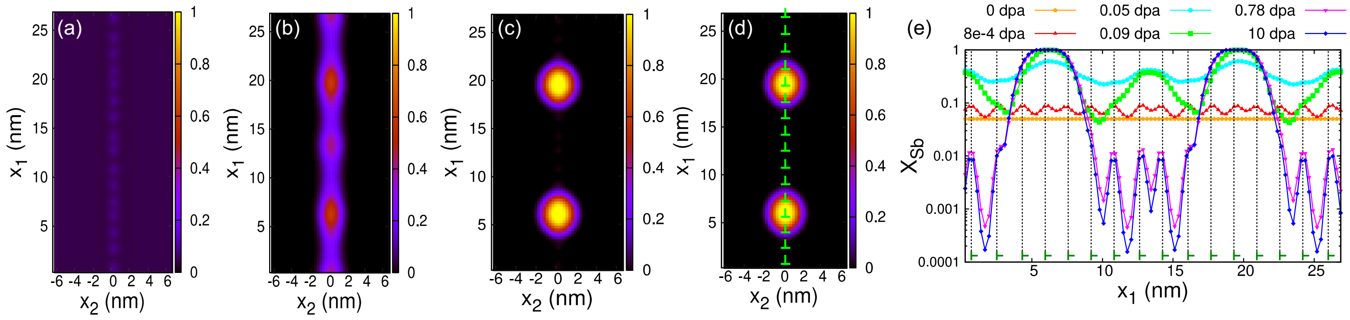

FIG. 2. Evolution of the Sb atomic fraction map for $\theta = 9.55°$ and $d = 13.44$ nm for (a) 8×10^{-4} dpa, (b) 0.05 dpa, (c) 0.78 dpa, (d) 10 dpa, and (e) the corresponding profiles along the GB. Dislocation cores are represented by inverted "T" symbols.

with two precipitates for $\theta = 9.55°$ and $d = 13.4$ nm, the total solute content in each precipitate remains largely constant up to 20 dpa, see Fig. S7. Some very slow coarsening may occur beyond that dose, although much longer simulations would be required to confirm it. The stability of the type 3 structures was further examined by switching off irradiation at some finite dose and subsequently annealing these structures using Eq. (1), but without sinks. In a first annealing scheme, vacancy concentrations were allowed to relax, resulting in nearly isotropic solute diffusion. In the second scheme, vacancy concentrations were kept fixed, thus retaining the anisotropic diffusion present during irradiation. For both annealing schemes, coarsening was soon observed; see examples for discrete and continuous GBs in Table S2 [27], as well as Fig. 4 in Appendix A. The characteristic times for coarsening, with respect to the slow evolution of the irradiated system up to 30 dpa, were accelerated in scheme 1 annealing by factors ≈ 1300 and ≈3000, for the above two GBs, respectively. These acceleration factors remain large, ≈200 and ≈150, even with scheme 2 annealing. It is thus concluded that diffusion anisotropy influences the stability of type 3 structures, but it is not the dominant factor inhibiting coarsening. More important, as we now discuss, is the convective flux arising from strong coupling between solutes and vacancies.

To understand these various results, we begin by considering the standard description of solid particle coarsening in the presence of convection [19,20]. Coarsening depends on the chemical Péclet number, but during irradiation Pe is neither uniform in space nor independent of time since solute segregation affects vacancy fluxes and vacancy concentrations, thus affecting both convection and diffusion. At early times, however, an analytical expression for a system-averaged Péclet number was derived, $\langle \mathrm{Pe} \rangle_o \approx (X_B K_0 d^2)/(\phi l_{VB}^V X_V^{\mathrm{irr}})$, where ϕ is the thermodynamic factor of the alloy, see Supplemental Material [27], Sec. SIIIA and Refs. [54–56]. Parametric phase field simulations confirm the scaling of $\langle \mathrm{Pe} \rangle_o$ with $(K_0 d^2)$, see Figs. S10 and S11, thus rationalizing the large effect that the grain size d has on stabilizing type 2 structures. Once solute redistribution takes place, the phase field simulation results are used to map out the relative strength of solute convection over solute diffusion using a local chemical Péclet number defined as $\mathrm{Pe}(\boldsymbol{x}, t) = |\nabla(\delta F/\delta X_V)|/|\nabla(\delta F/\delta X_B)|$, see Sec. SIII.B [27]. Far from the GB, Pe ≈ 1, as solute advection by radiation-induced segregation (RIS) is balanced by back thermal diffusion. Close to the precipitate-matrix interfaces, diffusion dominates over convection, resulting in Pe < 1, as expected [20] (see an illustrative example Fig. S8). In type 3 structures, however, Pe reaches large values between precipitates near dislocation cores, see Fig. 3(b), as these sinks draw large advection currents, while D_B^{GB} is small, recall, $D_B^{\mathrm{GB}} \approx D_B^{\mathrm{eq}}$. Moreover, maps of solute concentrations, e.g., Figs. 3(a) and 3(c), reveal two remarkable features along the GB: (i) The solute concentration far exceeds the bulk solubility limit, here by up to 2 orders of magnitude; and (ii) no significant capillary effects can be detected, i.e., the solute profile just outside the precipitate-matrix interface does

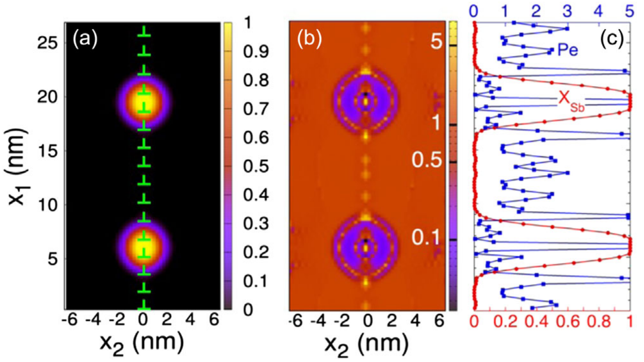

FIG. 3. Maps of (a) solute atomic fraction X_{Sb} and (b) Péclet number P_e for STGB with $\theta = 9.55°$ and $d = 13.44$ nm at 10 dpa. (c) Profiles of X_{Sb} (lower horizontal axis, red color online) and Pe (upper horizontal axis, blue color online) along x_1 on the GB ($x_2 = 0$), truncated at Pe ≤ 5 for clarity; the high value of Pe at the center of precipitate is due to the vanishingly small diffusion imposed by symmetry. The x_1 vertical axis is the same for (a), (b), and (c). See maps and profiles in Supplemental Material, Fig. S9 [27].

not depend on precipitate size. We thus conclude that local equilibrium is not met at these interfaces, in contrast to previous studies in solid-liquid systems, where, even for large Pe numbers, it was assumed that local equilibrium and Gibbs-Thomson capillary effects would be preserved [19,20].

The above results lead us to propose that the high value of Pe along the GB, between precipitates, is the determinant factor for the stabilization of type 3 structures. Specifically, we define two characteristic lengths (see Fig. 5 in Appendix B): (i) The diffusional boundary layer thickness δ_{DBL} as the radial distance between the precipitate-matrix interface, i.e., $X_B = 0.5$, and the point where $\mathrm{Pe} = 1$; and (ii) the precipitate-matrix interface width, δ_{PM}, using a 10%–90% criterion. It is observed that in type 3 structures, $\delta_{\mathrm{DBL}} < \delta_{\mathrm{PM}}/2$, i.e., that convection dominates over diffusion before the solute concentration reaches its matrix value. It is hypothesized that this inequality is a sufficient condition for fully suppressing capillary effects, and thus for triggering arrested coarsening. This hypothesis was tested by suddenly increasing X_V^{eq} in type 3 structures to increase GB diffusivity while reducing convection (recall that X_V^{eq} is the imposed concentration in the sink capture zone). Coarsening was then clearly observed, and $\delta_{\mathrm{DBL}} > \delta_{\mathrm{PM}}/2$ in these cases, thus supporting the above rationalization. For instance, upon increasing X_V^{eq} from 1.5×10^{-9} to 10^{-6}, an additional low dose of 1.1 dpa led to the full dissolution of one of the three precipitates shown in Fig. S5 [27] for the continuous GB sink, and already for 0.035 dpa we measured $\delta_{\mathrm{DBL}} = 6.84b$ and $\delta_{\mathrm{PM}}/2 = 2.44b$.

Returning now to the emergent length scale of type 3 structures, results from Table I indicate that this patterning length scale λ_P increases continuously with the strength of solute drag over back diffusion, until a continuous precipitate film forms on the GB. The dependence of λ_P with physical parameters might be assessed by modeling the dependence of δ_{DBL} and δ_{PM} with these parameters, but this is left for future work.

The present 2D simulation results provide a framework to anticipate the type 3 structures that could form in 3D systems. For example, at low Pe number, a Rayleigh-Plateau instability, which does not take place in 2D systems [57], could destabilize continuous tubular precipitates along GB dislocations, resulting in individual precipitates decorating GBs. This instability, and possibly the coarsening of precipitates, would be promoted by fast diffusion along dislocation cores. Isolated dislocations, on the other hand, could develop larger Pe numbers near their cores for purely geometrical reasons. For low GB misorientations, larger RIS solute advection could thus promote the stabilization of tubular precipitate structures. Testing these predictions is again left for future work.

While the present results do not include ballistic mixing, they should nevertheless approximate irradiation situations employing light ions, such as protons or energetic (MeV) electrons, as atomic transport arises primarily from defect mobility and not from recoil collisions. To the best of our knowledge there is no direct experimental evidence that irradiation could induce precipitate patterning at GBs. It is worth noting that solute precipitate structures have recently been observed at misfit dislocations and interfaces [32,58,59]. These structures, however, were rationalized as resulting from equilibrium segregation followed by spinodal decomposition [58] or from equilibrium wetting at misfit dislocation intersections [59], in contrast to the nonequilibrium kinetic stabilization identified here. The present work suggests that different GBs may respond differently since their distinct structures will affect their defect sink properties and diffusion coefficients D_B^{GB}. For example D_B^{GB} may be greatly enhanced relative to that of perfect STGBs used here. Structural disorder introduced by irradiation at GBs [60] may, however, reduce this variability. Last, it is envisioned that other nonequilibrium systems with internal sinks are susceptible to similar self-organization reactions in the presence of convective flows, e.g., battery electrodes during charging or discharging cycles, or alloys subjected to severe plastic deformation.

The research was supported by the U.S. Department of Energy, Office of Science, Basic Energy Sciences, under Award No. DE-SC0019875. This work made use of the Illinois Campus Cluster, a computing resource that is operated by the Illinois Campus Cluster Program (ICCP) in conjunction with the National Center for Supercomputing Applications (NCSA) and which is supported by funds from the University of Illinois at Urbana-Champaign. Stimulating discussions with Dr. Charles Schroder and Dr. Peter Voorhees are gratefully acknowledged.

All authors contributed significantly to the work. The primary contributions are as follows. G. F. B. M. carried out the research and analyzed the results. R. S. A. and P. B. conceptualized the work. L. T. developed the phase field code.

Appendix A: Effect of switching off irradiation.—The effect of turning off irradiation after reaching arrested coarsening was investigated in order to confirm that convection, i.e., irradiation-induced solute drag, was responsible for arrested coarsening. Several of the structures listed in Table I were investigated, including both STGBs and continuous GBs. In all cases local interface equilibrium and capillary effects were quickly recovered upon switching off irradiation, see Fig. 4, and coarsening was observed. Notice in particular the clear

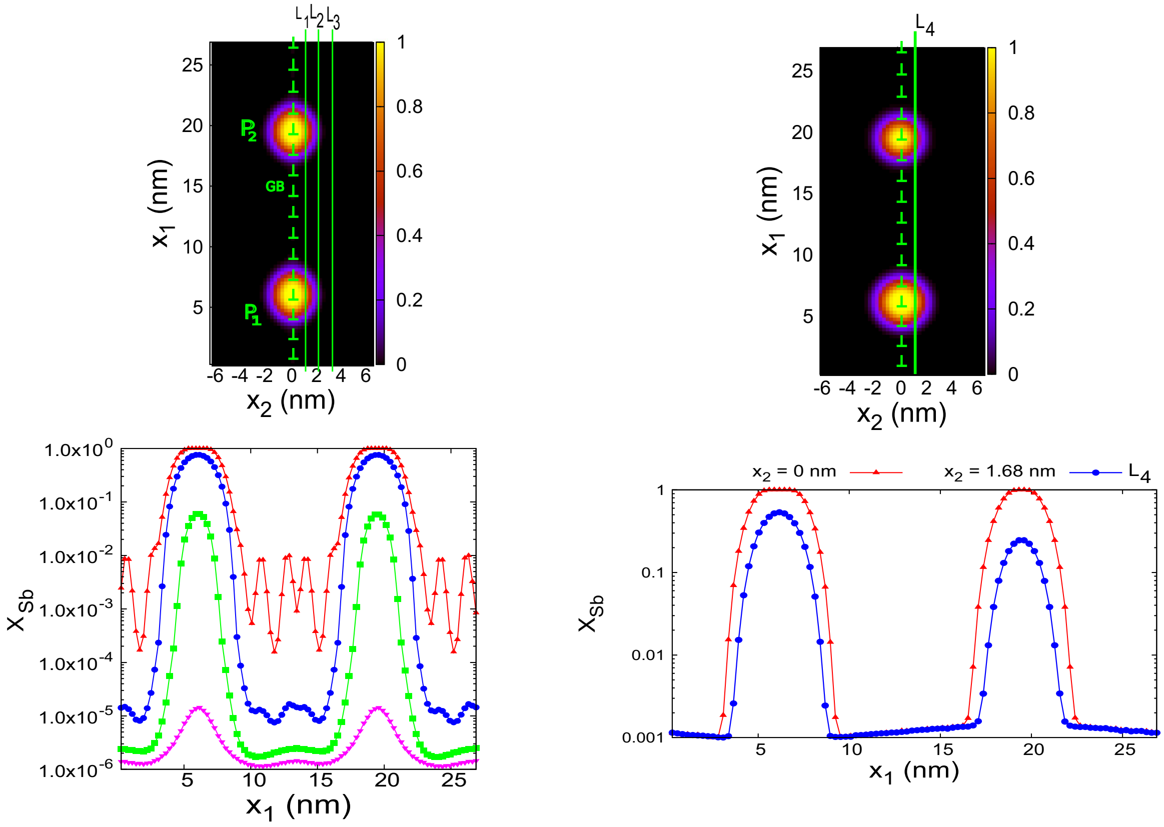

FIG. 4. Compositional solute maps (top row) and compositional profiles (bottom row) for the STGB shown in Fig. 3 in the state of arrested coarsening after irradiation for 10 dpa (left column) and after irradiation has been turned off and the system has been annealed for a short time, 35 sec, i.e., corresponding to an equivalent dose increment of 0.035 dpa (right column). During thermal annealing both X_{Sb} and X_v were evolved, thus corresponding to the annealing scheme 1 defined in the main text.

dependence of matrix solubility with precipitate curvature in the right column in Fig. 4, consistent with a Gibbs-Thomson effect, and the absence of such dependence under irradiation, see left column. Furthermore, the solute matrix solubility for the larger precipitate is now near its equilibrium value of 1.75×10^{-4}. Last, the precipitate shapes, which were anisotropic and elongated along the GB during arrested coarsening, became circular during annealing. See information related to the kinetics of coarsening after switching off irradiation in Supplemental Material Table S2 [27].

Appendix B: Length scales for rationalization of arrested coarsening.—It is proposed in the main text that a sufficient condition for arrested coarsening to take place is that the diffusional boundary layer thickness δ_{DBL} be smaller than the half-interface width $\delta_{\mathrm{PM}}/2$. These two length scales, defined in the main text, are illustrated below on an example that corresponds to the top precipitate, centered at $x_1 = 19$ nm, in Fig. 3. In this example, $\delta_{\mathrm{DBL}} = 0.60$ nm while $\delta_{\mathrm{PM}}/2 = 0.71$ nm, thus the condition $\delta_{\mathrm{DBL}} < \delta_{\mathrm{PM}}/2$ is indeed met.

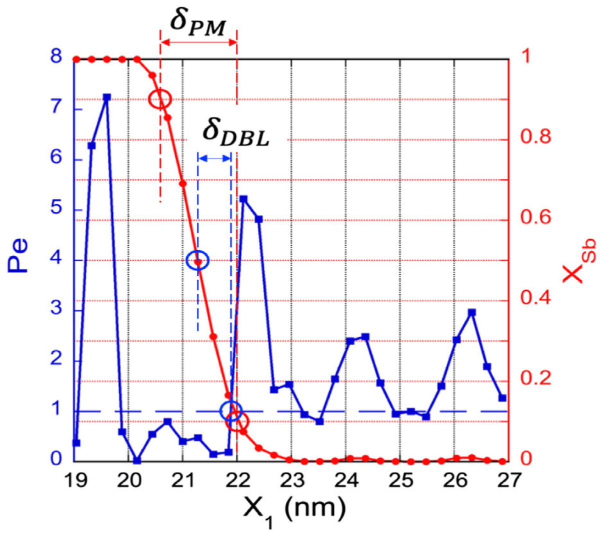

FIG. 5. Illustration of the definition of the diffusional boundary layer δ_{DBL} and of the interfacial width δ_{PM} for the top precipitate shown in Fig. 3. The blue and red empty circle symbols correspond to the radial distances used to define these length scales, from the middle of the interface to the point where $\mathrm{Pe} = 1$ for δ_{DBL}; and from $X_{\mathrm{Sb}} = 90\%$ to $X_{\mathrm{Sb}} = 10\%$ for δ_{PM}.

[1] G. Nicolis and I. Prigogine, *Self-Organization in Nonequilibrium Systems: From Dissipative Structures to Order through Fluctuations* (Wiley, New York, 1977).

[2] H. Haken, Synergetics: An Introduction (Springer Berlin, Heidelberg, 1983), 10.1007/978-3-642-88338-5.

[3] M. C. Cross and P. C. Hohenberg, Pattern formation outside of equilibrium, Rev. Mod. Phys. **65**, 851 (1993).

[4] N. Ghoniem and D. Walgraef, *Instabilities and Self-Organization in Materials: Volume I: Fundamentals of Nanoscience, Volume II: Applications in Materials Design and Nanotechnology* (Oxford University Press, Oxford, 2008).

[5] R. S. Nelson, J. A. Hudson, and D. J. Mazey, The stability of precipitates in an irradiation environment, J. Nucl. Mater. **44**, 318 (1972).

[6] W. Jäger and H. Trinkaus, Defect ordering in metals under irradiation, J. Nucl. Mater. **205**, 394 (1993).

[7] P. Bellon and R. S. Averback, Nonequilibrium Roughening of Interfaces in Crystals under Shear: Application to Ball Milling, Phys. Rev. Lett. **74**, 1819 (1995).

[8] S. Zghal, R. Twesten, F. Wu, and P. Bellon, Electron microscopy nanoscale characterization of ball milled Cu-Ag powders. Part II: Nanocomposites synthesized by elevated temperature milling or annealing, Acta Mater. **50**, 4711 (2002).

[9] M. Pouryazdan, B. J. P. Kaus, A. Rack, A. Ershov, and H. Hahn, Mixing instabilities during shearing of metals, Nat. Commun. **8**, 1611 (2017).

[10] J. H. Evans, Observations of a regular void array in high purity molybdenum irradiated with 2 MeV nitrogen ions, Nature (London) **229**, 403 (1971).

[11] Y. Gao, Y. Zhang, D. Schwen, C. Jiang, C. Sun, and J. Gan, Formation and self-organization of void superlattices under irradiation: A phase field study, Materialia **1**, 78 (2018).

[12] R. S. Averback, P. Bellon, and S. J. Dillon, Phase evolution in driven alloys: An overview on compositional patterning, J. Nucl. Mater. **553**, 153015 (2021).

[13] S. Berti, G. Boffetta, M. Cencini, and A. Vulpiani, Turbulence and Coarsening in Active and Passive Binary Mixtures, Phys. Rev. Lett. **95**, 224501 (2005).

[14] P. Perlekar, R. Benzi, H. J. H. Clercx, D. R. Nelson, and F. Toschi, Spinodal Decomposition in Homogeneous and Isotropic Turbulence, Phys. Rev. Lett. **112**, 014502 (2014).

[15] L. Ó Náraigh, S. Shun, and A. Naso, Flow-parametric regulation of shear-driven phase separation in two and three dimensions, Phys. Rev. E **91**, 062127 (2015).

[16] X. Fu, L. Cueto-Felgueroso, and R. Juanes, Thermodynamic coarsening arrested by viscous fingering in partially miscible binary mixtures, Phys. Rev. E **94**, 033111 (2016).

[17] H. Massana-Cid, D. Levis, R. J. H. Hernández, I. Pagonabarraga, and P. Tierno, Arrested phase separation in chiral fluids of colloidal spinners, Phys. Rev. Res. **3**, L042021 (2021).

[18] N. Akaiwa, S. C. Hardy, and P. W. Voorhees, The effects of convection on Ostwald ripening in solid-liquid mixtures, Acta Metall. Mater. **39**, 2931 (1991).

[19] L. Ratke and W. K. Thieringer, The influence of particle motion on Ostwald ripening in liquids, Acta Metall. **33**, 1793 (1985).

[20] L. Ratke and P. W. Voorhees, *Growth and Coarsening: Ostwald Ripening in Material Processing* (Springer, Berlin, 2002).

[21] P. Bai, D. A. Cogswell, and M. Z. Bazant, Suppression of phase separation in $LiFePO_4$ nanoparticles during battery discharge, Nano Lett. **11**, 4890 (2011).

[22] S. Odunuga, Y. Li, P. Krasnochtchekov, P. Bellon, and R. S. Averback, Forced Chemical Mixing in Alloys Driven by Plastic Deformation, Phys. Rev. Lett. **95**, 045901 (2005).

[23] D. Schwen, M. Wang, R. S. Averback, and P. Bellon, Compositional patterning in immiscible alloys subjected to severe plastic deformation, J. Mater. Res. **28**, 2687 (2013).

[24] M. Ghaly and R. S. Averback, Effect of Viscous Flow on Ion Damage near Solid Surfaces, Phys. Rev. Lett. **72**, 364 (1994).

[25] K. Nordlund, J. Keinonen, M. Ghaly, and R. S. Averback, Coherent displacement of atoms during ion irradiation, Nature (London) **398**, 49 (1999).

[26] C. C. Umbach, R. L. Headrick, and K.-C. Chang, Spontaneous Nanoscale Corrugation of Ion-Eroded SiO_2: The Role of Ion-Irradiation-Enhanced Viscous Flow, Phys. Rev. Lett. **87**, 246104 (2001).

[27] See Supplemental Material at http://link.aps.org/supplemental/10.1103/PhysRevLett.131.056201 for model parametrization, additional simulations results and expressions for global and local Péclet numbers.

[28] P. R. Okamoto and H. Wiedersich, Segregation of alloying elements to free surfaces during irradiation, J. Nucl. Mater. **53**, 336 (1974).

[29] A. J. Ardell and P. Bellon, Radiation-induced solute segregation in metallic alloys, Curr. Opin. Solid State Mater. Sci. **20**, 115 (2016).

[30] M. Nastar and F. Soisson, in *Comprehensive Nuclear Materials*, 2nd ed., edited by R. J. M. Konings and R. E. Stoller (Elsevier, Oxford, 2020), p. 235.

[31] A. Barbu and A. J. Ardell, Irradiation-induced precipitation in Ni-Si alloys, Scr. Metall. Mater. **9**, 1233 (1975).

[32] Q. Barrès, O. Tissot, E. Meslin, I. Mouton, B. Arnal, M. Loyer-Prost, and C. Pareige, Effect of grain boundary planes on radiation-induced segregation (RIS) at near Σ3 grain boundaries in Fe-Cr alloy under ion irradiation, Mater. Charact. **184**, 111676 (2022).

[33] E. Martínez, O. Senninger, A. Caro, F. Soisson, M. Nastar, and B. P. Uberuaga, Role of Sink Density in Nonequilibrium Chemical Redistribution in Alloys, Phys. Rev. Lett. **120**, 106101 (2018).

[34] R. K. Koju and Y. Mishin, Atomistic study of grain-boundary segregation and grain-boundary diffusion in Al-Mg alloys, Acta Mater. **201**, 596 (2020).

[35] P. Bellon and L. Thuinet, in *Comprehensive Nuclear Materials*, 2nd ed., edited by R. J. M. Konings and R. E. Stoller (Elsevier, Oxford, 2020), p. 779.

[36] J. B. Piochaud, M. Nastar, F. Soisson, L. Thuinet, and A. Legris, Atomic-based phase-field method for the modeling of radiation induced segregation in Fe-Cr, Comput. Mater. Sci. **122**, 249 (2016).

[37] G. A. Khachaturyan, *Theory of Structural Transformations in Solids* (Wiley, New York, 1983).

[38] G. Martin, Phase stability under irradiation: Ballistic effects, Phys. Rev. B **30**, 1424 (1984).

[39] R. A. Enrique and P. Bellon, Compositional Patterning in Systems Driven by Competing Dynamics of Different Length Scale, Phys. Rev. Lett. **84**, 2885 (2000).

[40] D. Simeone, G. Demange, and L. Luneville, Disrupted coarsening in complex Cahn-Hilliard dynamics, Phys. Rev. E **88**, 032116 (2013).

[41] L. Luneville, P. Garcia, and D. Simeone, Predicting Nonequilibrium Patterns beyond Thermodynamic Concepts: Application to Radiation-Induced Microstructures, Phys. Rev. Lett. **124**, 085701 (2020).

[42] Q. Li, R. S. Averback, and P. Bellon, Compositional patterning in irradiated alloys: Effective potentials and effective interfacial energy, Phys. Rev. B **103**, 104110 (2021).

[43] D. Carpentier, T. Jourdan, Y. Le Bouar, and M. C. Marinica, Effect of saddle point anisotropy of point defects on their absorption by dislocations and cavities, Acta Mater. **136**, 323 (2017).

[44] A. J. McAlister, The Al-Sb (aluminum-antimony) system bulletin of alloy, Phase Diagrams **5**, 462 (1984).

[45] T. Schuler, D. R. Trinkle, P. Bellon, and R. Averback, Design principles for radiation-resistant solid solutions, Phys. Rev. B **95**, 174102 (2017).

[46] J. W. Cahn and J. E. Hilliard, Free energy of a nonuniform system. I. Interfacial free energy, J. Chem. Phys. **28**, 258 (1958).

[47] H. Emmerich, Advances of and by phase-field modelling in condensed-matter physics, Adv. Phys. **57**, 1 (2008).

[48] N. Moelans, B. Blanpain, and P. Wollants, An introduction to phase-field modeling of microstructure evolution, CALPHAD: Comput. Coupling Phase Diagrams Thermochem. **32**, 268 (2008).

[49] I. Steinbach, Phase-field model for microstructure evolution at the mesoscopic scale, Annu. Rev. Mater. Res. **43**, 89 (2013).

[50] H. Ullmaier, Atomic defects in metals group III, Vol. 25, Int. J. Mat. Res. **84**, 211 (1993).

[51] H. Wu, T. Mayeshiba, and D. Morgan, High-throughput ab-initio dilute solute diffusion database, Sci. Data **3**, 160054 (2016).

[52] T. Schuler, L. Messina, and M. Nastar, KINECLUE: A kinetic cluster expansion code to compute transport coefficients beyond the dilute limit, Comput. Mater. Sci. **172**, 109191 (2020).

[53] A. B. Sivak, V. M. Chernov, V. A. Romanov, and P. A. Sivak, Kinetic Monte-Carlo simulation of self-point defect diffusion in dislocation elastic fields in bcc iron and vanadium, J. Nucl. Mater. **417**, 1067 (2011).

[54] H. Wiedersich, P. R. Okamoto, and N. Q. Lam, A theory of radiation-induced segregation in concentrated alloys, J. Nucl. Mater. **83**, 98 (1979).

[55] R. Sizmann, The effect of radiation upon diffusion in metals, J. Nucl. Mater. **69–70**, 386 (1978).

[56] L. Huang, M. Nastar, T. Schuler, and L. Messina, Multiscale modeling of the effects of temperature, radiation flux, and sink strength on point-defect and solute redistribution in dilute Fe-based alloys, Phys. Rev. Mater. **5**, 033605 (2021).

[57] M. San Miguel, M. Grant, and J. D. Gunton, Phase separation in two-dimensional binary fluids, Phys. Rev. A **31**, 1001 (1985).

[58] M. Kuzmina, M. Herbig, D. Ponge, S. Sandlöbes, and D. Raabe, Linear complexions: Confined chemical and structural states at dislocations, Science **349**, 1080 (2015).

[59] D. Chen, N. Li, D. Yuryev, J. K. Baldwin, Y. Wang, and M. J. Demkowicz, Self-organization of helium precipitates into elongated channels within metal nanolayers, Sci. Adv. **3**, eaao2710 (2017).

[60] C. M. Barr, E. Y. Chen, J. E. Nathaniel, P. Lu, D. P. Adams, R. Dingreville, B. L. Boyce, K. Hattar, and D. L. Medlin, Irradiation-induced grain boundary facet motion: *In situ* observations and atomic-scale mechanisms, Sci. Adv. **8**, eabn0900 (2022).